Applied Physics A (2022) 128:540
https://doi.org/10.1007/s00339-022-05653-3

Applied Physics A
Materials Science & Processing

Crystal structure, morphology and magnetic properties of nanocrystalline Zr_6Fe_{23} thin films grown on Si(001) substrate

R. Fersi[1,3] · **A. P. Dalia**[2]

Received: 13 January 2022 / Accepted: 25 April 2022 / Published online: 31 May 2022

Abstract

In this paper, crystal structure, morphology and magnetic properties of nanocrystalline Zr_6Fe_{23} thin films have been reported. Zr_6Fe_{23} films with different thickness X were grown by RF magnetron sputtering onto Si(001) substrate. The X thickness varies from 18 to 500 nm. From grazing X-ray diffraction patterns (GIXRD), the Zr_6Fe_{23}/Si(001) films have a single phase with cubic structure Th_6Mn_{23} type (Fm-3m space group) structure. We showed the presence of a strong preferred orientation (4 4 0) for X between 18 and 402 nm. However, for higher thicknesses $X \geq 402$ nm, multiple peaks are observed show the polycrystalline nature of the films and textured along (4 4 2), (5 3 3) and (6 6 0) orientations. The magnetic properties were affected by the thickness due to the morphology, roughness R_{rms} and intergrain exchange coupling (IEC). The correlations between these properties are investigated using the magnetic force microscopy (MFM) analysis. The 200 nm-thick Zr_6Fe_{23}/Si(001) film showed a high coercivity $H_c = 3580$ Oe, maximum energy product $(BH)_{max}$ of 2.45 MGOe, magnetic anisotropy field $H_a = 11230$ Oe and Curie temperature $T_C \simeq 821$ K. The results found in this work could potentially pave the way for the future exploration and of magnetic recording development or spintronic devices made from nanocrystalline Zr_6Fe_{23} films.

Keywords Nanocrystalline Zr_6Fe_{23}/Si(001) film · Microstructural properties · Magnetic properties · MFM analysis

1 Introduction

Nowadays, the magnetic materials have taken much interest because of their potential applications in various magnetic technologies. Among these materials, the nanocrystalline powders and thin films based on transition metals (Fe, Co, Ni ...) have received a lot of attention, due to their interesting magnetic properties and their performance [1–5]. In particular, the nanocrystalline ZrCo or ZrNi alloys have been used in several applications including magnetic recording, spintronic devices and magneto-optical switches [6–10]. In this context, the $ZrFe_x$ alloy seems a good promising for many applications, due to the possibility of adjusting and optimizing its magnetic properties by varying the Fe concentration x and the preparation conditions. In the binary Zr–Fe system, several compounds are formed: Zr_2Fe, Zr_3Fe, Zr_4Fe, Zr_6Fe_{23} and $ZrFe_2$ which have quite diverse structural and magnetic properties [11, 12]. These compounds exhibit ferromagnetic behavior and excellent intrinsic magnetic properties as Curie temperature T_C, the magnetocrystalline anisotropy H_A and a important saturation magnetization M_s [13, 14]. Little quantitative information on the magnetic properties of Zr_6Fe_{23} alloys has been reported. From the phase diagram of the Zr–Fe system [15], the Zr_6Fe_{23} phase can exist only in a very narrow range where the Zr atomic composition is between 26 % and 31 %, and can be obtained in the temperature range from 1173 K to 1756 K . The Zr_6Fe_{23} compound crystallize in the Th_6Mn_{23}-type cubic structure with Fm-3m space group. The lattice parameters are $a = b = c = 8.2662$ Å. The Zr atoms occupy the crystallographic 24e sites while Fe atoms occupy two 32f sites, 24d and 4e sites [16, 17]. The Zr_6Fe_{23} compound has the highest T_C compared to other ZrFe compounds. The T_C is around 821 K, a saturation magnetostriction λ_{Ms} of 8×10^{-6} and magnetic moment per Fe atom is 1.65 μ_B at 300 K and 1.876 μ_B at 5 K [13]. These magnetic properties suggest that

---

✉ R. Fersi
riadh.fersi@fst.utm.tn

[1] Laboratoire Matériaux Organisation et Propriétés, Faculté des Sciences de Tunis, Université de Tunis El Manar, Tunis 2092, Tunisia

[2] Department of Materials Science and Engineering, 313 Splaiul Unirii Street, 020745 Bucharest, Romania

[3] LMOP, Département de Physique, Faculté des Sciences de Tunis, Campus Universitaire, El Manar Tunis 2092, Tunisie

the films of Zr_6Fe_{23} compound may also have significant magnetic properties. Much less works has been devoted thin Zr–Fe films. In particular, mainly films with low Zr concentration have been studied [19–23]. We could only find few studies reports of Zr-rich epitaxial films, although no evidence of epitaxial growth of the film has been given.

In this article, we present a systematic study of crystal structure, morphology and magnetic properties of Zr_6Fe_{23} alloy thin films grown on Si(001) substrate by RF magnetron sputtering. The correlation between the microstructure, exchange interaction and magnetic anisotropy properties is discussed, using the magnetic force microscopy (MFM) analysis.

2 Elaboration and characterization methods

2.1 Elaboration and characterization methods of Zr_6Fe_{23}/Si(001) films

Zr_6Fe_{23} films were grown by radio frequency (RF) magnetron sputtering deposition technique (Fig. 1) from nanocrystalline Zr_6Fe_{23} compact powders (§ Section 3.1). The Zr_6Fe_{23} thin films were prepared on Si(001) substrates sized [20×10^{-2} m] × [20×10^{-2} m] with about 2×10^{-2} m thickness. The distance from the target to the substrate was 15×10^{-2} m throughout. A power supply operated at a crystal-controlled frequency of 13.60 MHz. The sputtering chamber was evacuated to a base pressure of 8×10^{-3} Pa using rotating and oil diffusion pumps. The deposition was done at constant RF power of 60 Watt at substrate temperature T_s of 873 K. The flow rates of the O_2 and Ar sputtering gases were set at a ratio of 2:8. The coatings were realized out from 15 min to 195 min leading to a variation in the Zr_6Fe_{23} thickness X from 18 to 500 nm. The RF power source was switched to a Au target to form a 20 nm-thick Au overlay layer on Zr_6Fe_{23} layers to prevent oxidation. The process parameters employed during deposition of Zr_6Fe_{23}/Si(001) films are listed in Table 1. The thickness measurement and structural characterization of Zr_6Fe_{23}/Si(001) films were determined by X-ray reflectivity and grazing incidence X-ray diffraction (GIXRD) techniques, respectively. The ex situ X-ray reflectivity with best fit theoretical curve measurements was performed using a Bruker 4-circle diffractometer equipped with a Cu-sealed tube point source and a Göbel Mirror optic to produce a 2D-collimated parallel beam. The incidence angle for GIXRD measurements has been fixed to 1° with 2θ varying from 20° to 90°. The surface morphologies, cross-sectional images were observed by scanning electron microscopy (SEM) coupled to energy-dispersive X-ray analysis (EDX). High-resolution transmission electron microscope (HRTEM) imaging was performed using Tecnai G2 F20 FEI TEM. The roughness R_{rms} was examined using atomic force microscopy (AFM, 3SPA-300HV). The magnetic properties are investigated by a physical property measurement system equipped with vibrating sample magnetometer (PPMS-VSM/Quantum Design, Dynacool 7), SQUID magnetometer and magnetic force microscopy (MFM).

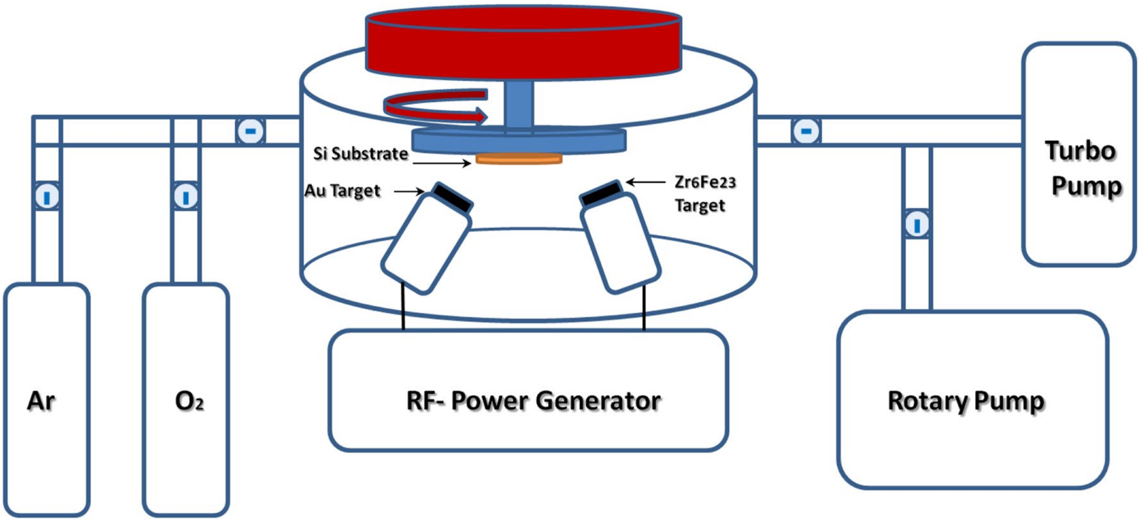

Fig. 1 Schematic diagram of the RF magnetron sputtering deposition technique used to elaborate the Zr_6Fe_{23}/Si(001) films

Table 1 Process parameters employed during the deposition of Zr_6Fe_{23}/Si(001) films

Parameters	Value
Target	Nanocrystalline Zr_6Fe_{23} powders
Substrate	Si(001)
Distance between substrate and target	15×10^{-2} m
Overlay layer (*X* thickness)	Au (*X* = 20 nm)
RF power	60 Watt
Sputtering gas pressure	0.7 Pa
Substrate temperature T_s	873 K
O_2/Ar ratio	2:8
Deposition time (*X* thickness)	15 min (18 nm), 32 min (48 nm)
	65 min (98 nm),90 min (149 nm)
	120 min (200 nm), 150 min (298 nm)
	175 min (402 nm), 195 min (500 nm)

3 Results and discussion

3.1 Microstructure and magnetic properties of nanocrystalline Zr_6Fe_{23} powders

The nanocrystalline Zr_6Fe_{23} powders were prepared by high-energy ball milling [24, 25]. After milling for 5 hours with ball to powder ratio of 15/1, under high-purity Ar atmosphere, the Zr_6Fe_{23} samples, enveloped in tantalum foil, are annealed for 72 hours in sealed silica tube under 10^{-4} Pa at different annealing temperature T_a from 800 to 1725 K. The crystal structures of Zr_6Fe_{23} sample were detected by X-ray diffraction (XRD) with CuK_α radiation. The pattern refinement was performed with the FULLPROF computing code based on the Rietveld technique [26–28]. The goodness-of-fit parameters χ^2 and R_B were used as numerical criteria to describe the quality of the fit between calculated and experimental XRD data [35, 36]. Figure 2a presents the Rietveld analysis result of XRD pattern of nanocrystalline Zr_6Fe_{23} powders annealed at 1425 K. The result of the structure refinement shows the presence of a main phase with the cubic Th_6Mn_{23} type structure (Fm-3m space group (No.225)). We note minor quantities of the oxide phases appearing due to selective oxidation of ZrO_2. The lattice parameters are $a = b = c = 8.2662$ Å. The Zr atoms occupy the crystallographic 24e sites while Fe atoms occupy two 32f sites, 24d and 4e sites. The lattice parameters, R_a and χ^2 factors from Rietveld fit are given in Table 2. These values of structural parameters are in agreement with the results obtained previously [16, 17]. The T_C temperature of Zr_6Fe_{23} compound was determined from the M(T) curve by extrapolating the linear part of the M(T) curve and finding the temperature value of the intersection with the extended baseline [18] (Fig. 2b). The T_C temperature is around 821 K. To study the extrinsic properties, we have optimized the Zr_6Fe_{23} microstructure, which can lead us to the best coercivity H_c. We have therefore used, for this compound, several annealing at different temperatures T_a. The optimum extrinsic magnetic properties are obtained for T_a = 1425 K: H_c = 9258 Oe, M_r = 39.9 emu/g and $(BH)_{max}$ = 4.92 MGOe. Figure 3 shows the hysteresis loop at 298 K, for the nanocrystalline Zr_6Fe_{23} sample annealed at 1425 K.

3.2 X-ray reflectivity of Zr_6Fe_{23}/Si(001) films

The X-ray reflectivity experiments have been realized on Zr_6Fe_{23}/Si(001) films for different thickness X. Figure 4 presents a typical example of X-ray reflectivity for X = 48 nm. The experimental X-ray reflectivity data were analyzed with the Diffrac Plus LEPTOS software [29]. Using a genetic algorithm [30], the best simulation suited to experimental data was performed by adjusting the parameters: film thickness X, density d* and root mean square roughness R_{rms} values. The found results from the X-ray reflectivity adjustment are listed in Table 3.

Table 2 *a*, *b* and *c* unit cell parameters, atomic positions, R_B and χ^2 factors, from Rietveld refinement of Zr_6Fe_{23} compound annealed at T_a = 1425 K

Cell parameters	$a = b = c = 8.2662$ Å
Sites	Atomic positions (x, y, z)
Zr_1(24e)	(0.296, 0, 0)
Fe_1(32f)	(0.122, 0.122, 0.122)
Fe_2(32f)	(0.322, 0.322, 0.322)
Fe_3(24d)	(0, 1/4, 1/4)
Fe_4(4a)	(0, 0, 0)
R_B	2.13
χ^2	2.84

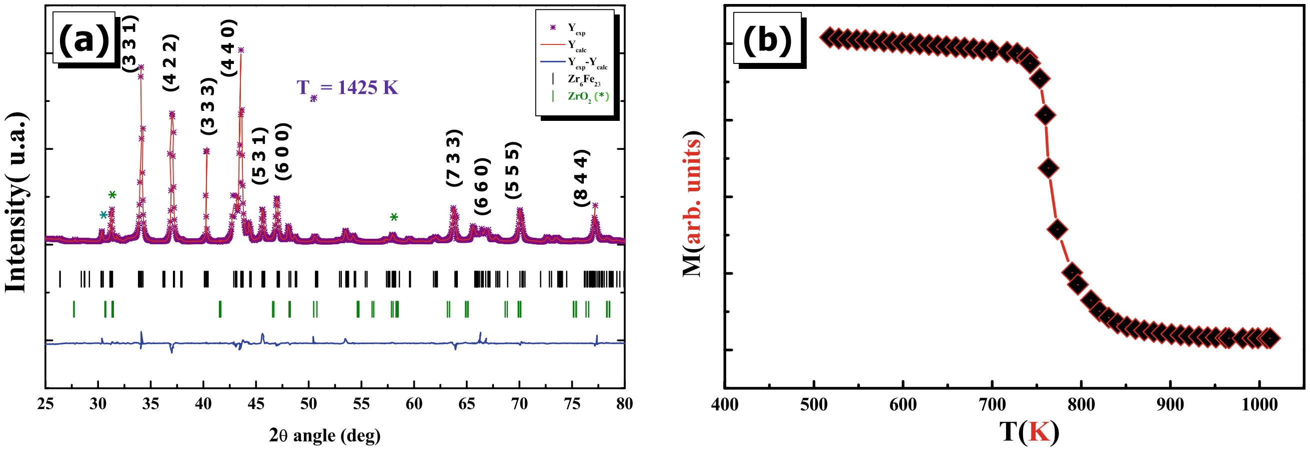

Fig. 2 **a** Rietveld analysis for X-ray diffraction patterns and **b** magnetization curve M(T) of nanocrystalline Zr_6Fe_{23} compound annealed at T_a = 1425 K

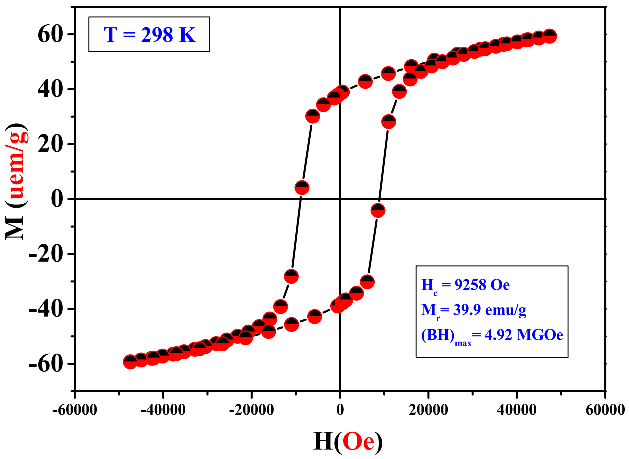

Fig. 3 Hysteresis loop of nanocrystalline Zr_6Fe_{23} compound annealed at T_a = 1425 K, measured at 298 K

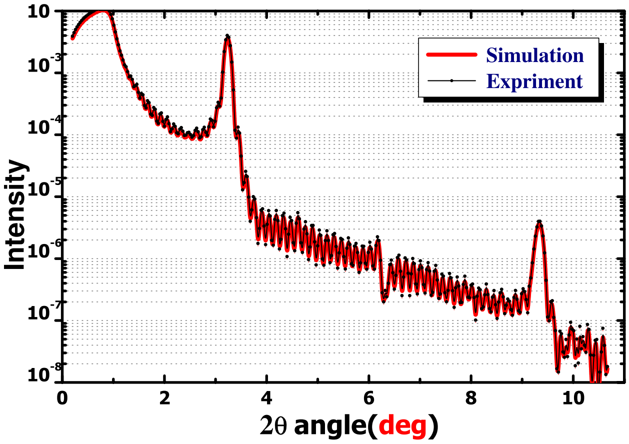

Fig. 4 Experimental X-ray reflectivity with best fit theoretical curve of Zr_6Fe_{23}/Si(001) for X = 48 nm

3.3 Crystal structure and morphology of Zr_6Fe_{23}/Si(001) films

The crystal structure of the thin layers was followed by Grazing Incidence X-ray Diffraction (GIXRD). Figure 5 shows the GIXRD patterns of Zr_6Fe_{23}/Si(001) films for different thickness X: 18 nm, 98 nm, 200 nm and 500 nm. No peak appeared for the thickness $X = 18$ nm. This layer consists of small grains oriented randomly due to the amorphous state of the Si(001) substrate, so no diffraction peak could be detected. For films with intermediate thickness (between 48 and 298 nm), we observed the presence of a single peak located at 43.2° was indexed as the (4 4 0) plane of the cubic structure Th_6Mn_{23} type (Fm-3m space group) of the phase Zr_6Fe_{23}. For these films, a strong (4 4 0) texture is evidenced. For the thickest films ($X \geq 400$ nm), we can see in addition to (4 4 0) peak, which increases in intensity with increasing X thickness, the appearance of secondary peaks located at positions: $2\theta =$ 36.1°, 52.2° and 69.3° corresponding respectively to the (4 4 2), (5 3 3) and (6 6 0) planes of Zr_6Fe_{23} structure. We conclude, that for the highest thickness, the films exhibit a polycrystalline structure. The grains size D was calculated for the intense diffraction peak (4 4 0) using Scherrer's equation [31–33]: $D = 0.9\lambda/\beta_2 \mathrm{Cos}\theta$, where $\lambda = 1.54$ Å is the wavelength of the incident X radiation, β_2 represents the full-width at half-maximum of the peaks at the diffraction angle θ [34, 35]. The grain sizes D of the Zr_6Fe_{23}/Si(001) films corresponding to (4 4 0) reflection have been found to increase with the increase of X thickness. The results calculated by Scherrer's equation show that, the average grain size D was 6 nm, 17 nm 28 nm, 39 nm, 49 nm, 82 nm, 105 nm, 111 nm, 120 nm for thickness $X = 18$ nm , $X = 48$ nm, $X = 98$ nm, $X = 149$ nm, $X = 200$ nm, $X = 249$ nm, $X = 298$ nm, $X = 402$ nm and $X = 500$ nm, respectively (Table 4). The increase in the grain size D as a function of d

Table 3 Thickness X(nm), root mean square roughness R_{rms} and density values d* of Zr_6Fe_{23}/Si(001) films obtained from the experimental XRR data simulation

Thickness X(± 2 nm)	18	48	98	149	200	249	298	402	500
R_{rms}(± 0.1 nm)	2.89	4.11	4.21	4.54	5.65	6.09	7.53	10.37	11.49
d*(± 0.2 g/cm^3)	7.60	7.60	7.59	7.59	7.59	7.58	7.58	7.58	7.59

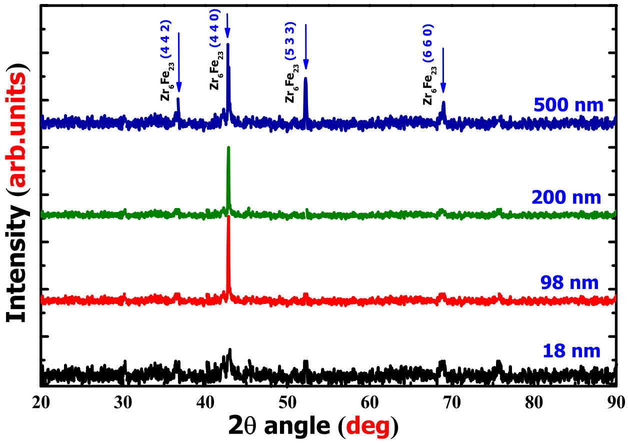

Fig. 5 GIXRD patterns for Zr_6Fe_{23}/Si(001) films with different thickness *X*: 18 nm, 98 nm, 200 nm and 500 nm

thickness is related to the increase in the magnetic domains (§ Section 3.4).

Figure 6a, b shows examples of SEM micrographs for samples with $X = 48$ nm and 500 nm. The micrographs clearly revealed the uniformity of the surfaces. The boundary Si/ZrFe and ZrFe/Au interfaces between the different layers Si, ZrFe, and Au and a relatively rough surface of all layers are clearly visible. Figure 7a presents the energy-dispersive X-ray spectroscopy (EDS) data analysis of Zr_6Fe_{23} layers. EDS analysis was performed by scanning field emission electron microscopy (FESEM). The atomic percentages of Zr and Fe, were 19.25 % and 78 %, respectively (Fig. 7a). We note the presence of some traces of oxidations (O) and impurities (C, Si, Au and Ni) with low atomic percentage. The Zr_6Fe_{23} stoichiometric proportions were roughly maintained. The composition distribution of the films was studied by STEM-EDX mapping (Fig. 7b). The Zr and Fe elements were distributed evenly in the surface mapping. The composition of Zr and Fe ranges from 19.5 to 21 % and 78 to 77 %, respectively. Figure 6.(a*) and (b*) shows the bright field images of the microstructure of Zr_6Fe_{23} films for $X = 48$ nm and 500 nm. The corresponding selected area electron diffraction (SAED) pattern exhibits bright diffraction rings, which are a typical characteristic of nanocrystalline phase [4, 37, 38]. Figure 6a** and b** shows the size distribution histograms for thickness $X = 48$ nm and 500 nm, respectively. The average grain size increased D from 6 to 120 nm with increasing X thickness from 18 to 500 nm. Figure 8 shows the surface morphologies (3D and 2D) for different thickness: $X = 18$ nm ((a), (a*)), $X = 98$ nm ((b), (b*)), $X = 200$ nm ((c), (c*) and $X = 500$ nm ((d), (d*)). From the AFM images analysis, we have extracted the root means square roughness R_{rms}. The values found are listed in Table 4. All Zr_6Fe_{23}/Si(001) films present a morphological structure composed of very tight grains, indicating a continuous surface. The grain size is in the nanometer range confirming the observation performed by the SEM microscopy. The R_{rms} increases with increasing *X* thickness and its value varies from 2.92 nm for $X = 18$ nm to 11.52 nm for $X = 500$ nm.

3.4 Magnetic and exchange interaction properties of Zr_6Fe_{23}/Si(001) films

The hysteresis loops of Zr_6Fe_{23}/Si(001) film for different X thickness are given in Fig. 9. It can be seen that the films exhibit different magnetic behaviors, and the magnetic properties are listed in Table 5. We note that H_c decreases with increasing thickness, except for 200 nm-thick film, where a maximum in the H_c vs X curve was observed ($H_c \simeq$ 3580 Oe). The minimum value of H_c, equal to 651 Oe, was obtained for the 500 nm-thick films. The evolution of H_c with thickness may be attributed to the surface roughness and grains morphology effect [41]. The films with smooth surfaces are characterized by large H_c. For X > 249 nm, the grain size D and surface roughness R_{rms} become large, range from 105 to 120 nm and 7.56 nm to 11.52 nm, respectively. This allows the appearance of crystalline defects, such as twins or grain boundaries and which contribute to the fall of H_c.

The intergrain exchange coupling analysis (IEC) between the magnetic particles was evaluated by measuring Henkel

Table 4 The roughness R_{rms} and grain size D for different thickness X

X(nm)	18	48	98	149	200	249	298	402	500
R_{rms}(nm)	2.92	4.13	4.24	4.57	5.68	6.13	7.56	10.38	11.52
D(nm)	6	17	28	39	49	82	105	111	120

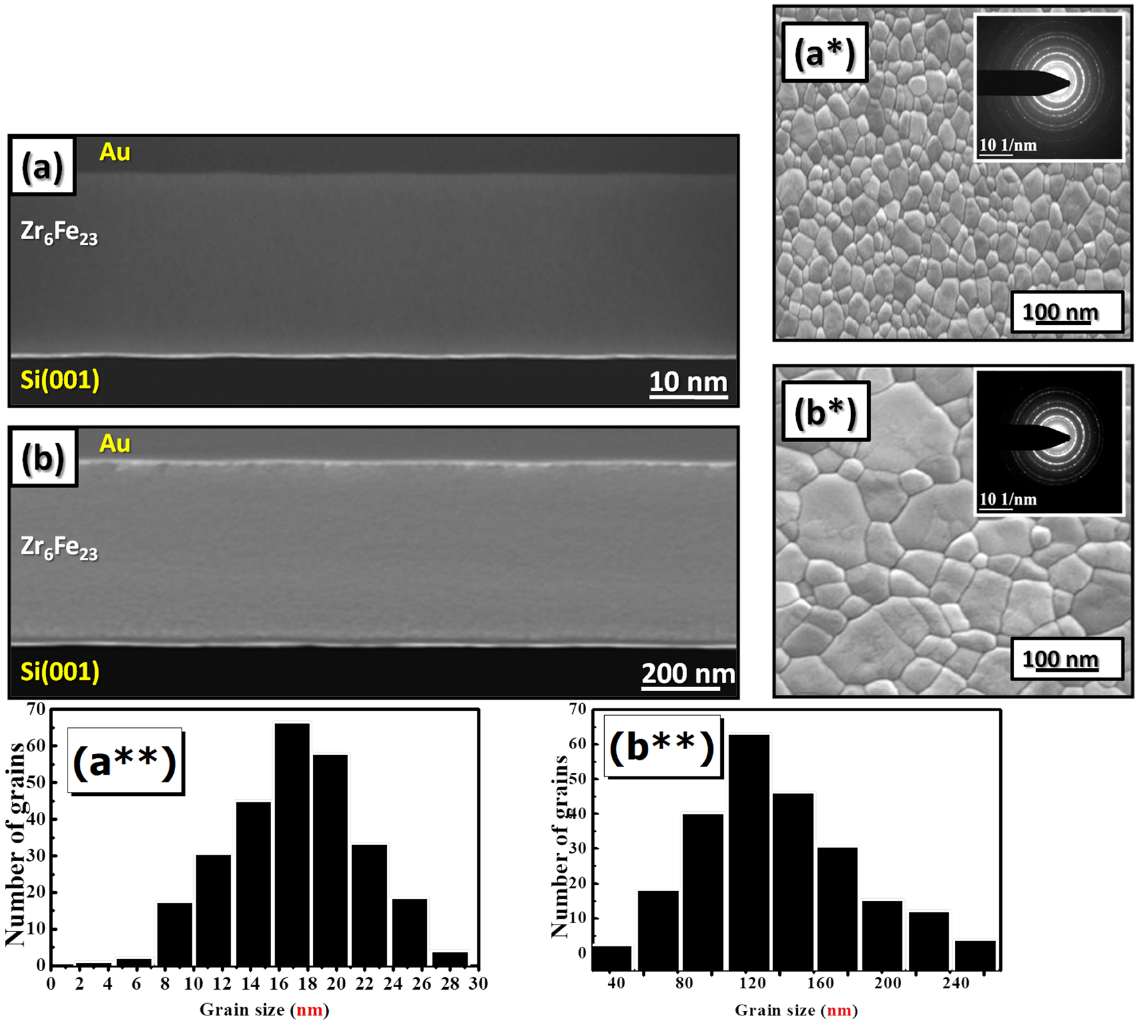

Fig. 6 SEM micrographs of Zr_6Fe_{23}/Si(001) films for thickness X = 48 nm (**a**) and 500 nm (**b**). ESEM micrographs of Zr_6Fe_{23}/Si(001) films for thickness X = 48 nm (**a***) and 500 nm (**b***). The size distribution histograms for thickness X = 48 nm (**a****) and 500 nm (**b****)

Fig. 7 **a** EDS pattern of Zr_6Fe_{23} films for X = 200 nm. **b** Elemental mapping of Zr_6Fe_{23}/Si(001) films for X = 200 nm

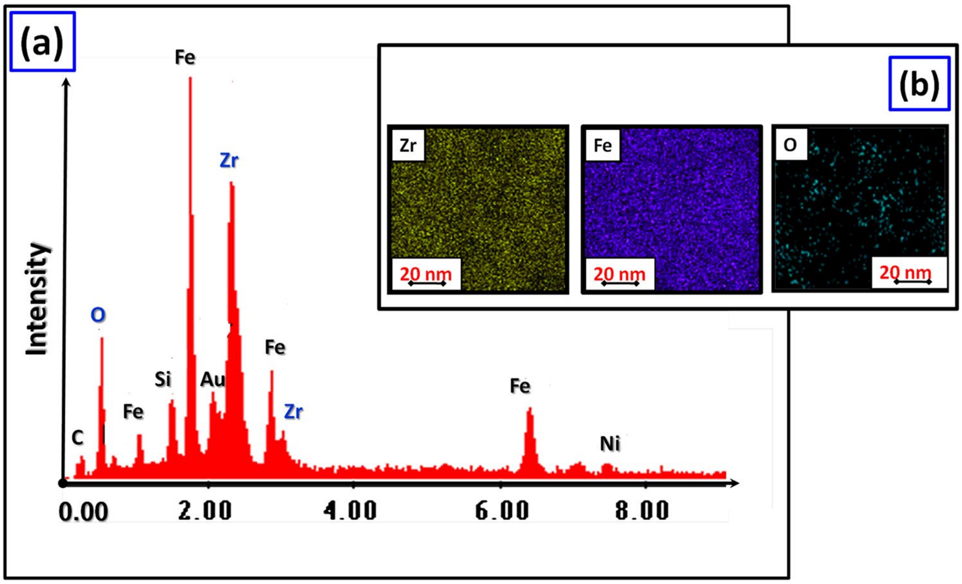

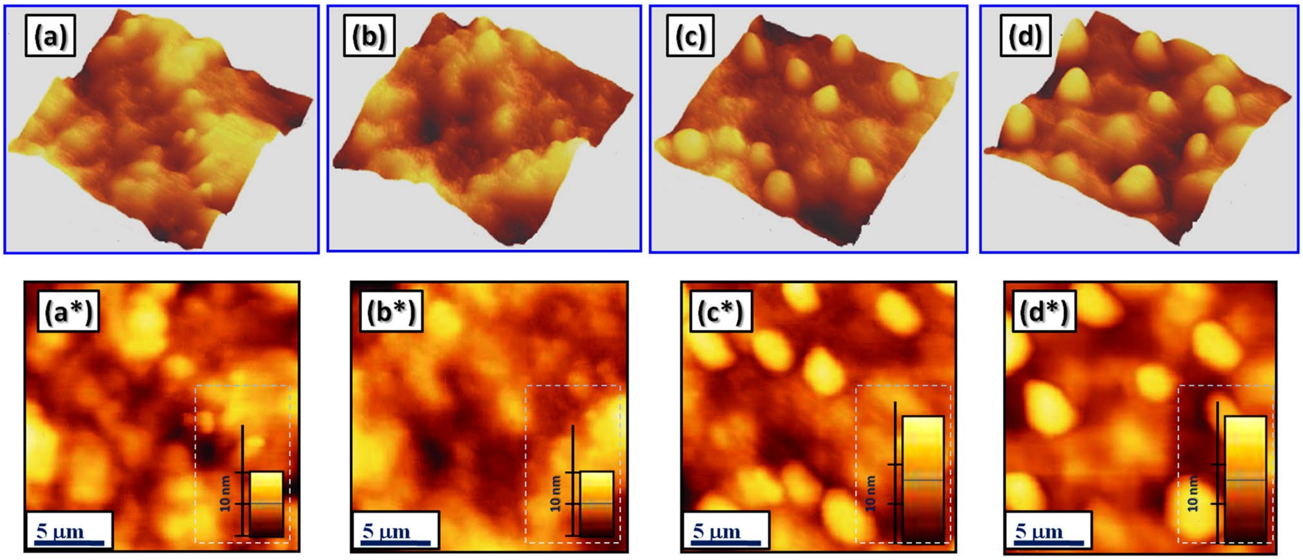

Fig. 8 AFM topographic images (3D and 2D) for Zr_6Fe_{23}/Si(001) films with different thickness X: X = 18 nm ((a), (a*)), X = 98 nm ((b), (b*)), X = 200 nm ((c), (c*)) and X = 500 nm ((d), (d*))

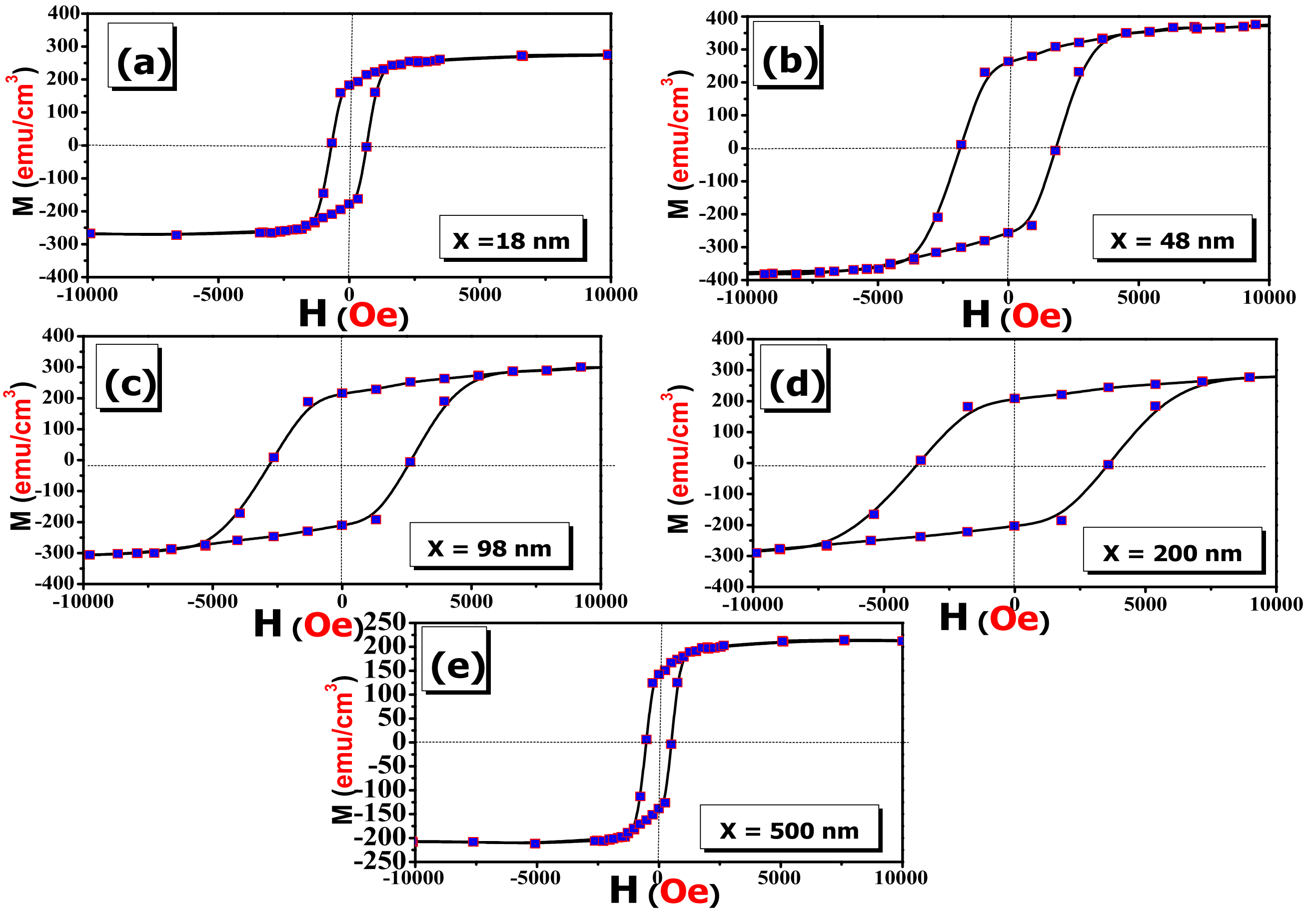

Fig. 9 **a** Hysteresis loops at room temperature of Zr_6Fe_{23}/Si(001) for different thickness X (X = 18 nm, 48 nm, 98 nm, 200 nm and 500 nm)

curves [42, 43]. The Δm*-H curves of Zr_6Fe_{23}/Si(001) films with different X thickness shown in Fig. 10a. It can be seen that the film with $X = 200$ nm possesses the higher positive peak value, which is in accordance with coercivity result. As the X thickness increases, the positive peak value for each of Δ m* plots (Δm* > 0) shows a "first increasing and then decreasing" tendency, which means that the thickness of Zr_6Fe_{23} layer has an impact on intergrain exchange coupling. The Δm*-H curve was determined by the relation [43]:

$$\Delta m^* = m_{init}(H) - \frac{1}{2}(m_{\uparrow}(H) + m_{\downarrow}(H)) \qquad (1)$$

where m_{init} is the initial magnetization curve. $m_{\uparrow}$ and $m_{\downarrow}$ are respectively the up (↑) and down (↓) parts of the hysteresis loop (H > 0). If,

- Δm* < 0, the magnetic dipolar interaction is predominant,
- Δm* > 0, the intergrain exchange coupling is dominant.

Figure. 10b shows the variation of the magnetization M(H) curves near saturation of Zr_6Fe_{23} films for different thickness X. The solid line presents the experimental data and theoretical simulation obtained using the expression [44–48]:

$$M(H) = M_s + a/H^2 \qquad (2)$$

H is the applied magnetic field. M_s is the saturation magnetization. The a coefficient is related to anisotropy field H_a, $a = -\frac{2}{105}H_a^2$. The different magnetic parameters obtained are listed in Table 6. The saturation magnetization M_s value increases from 278 emu/cm^3 at X = 18 nm to 312 emu/cm^3 at X = 200 nm. Same behavior for anisotropy constant H_a evolution, the H_a value increases from 10100 Oe to a maximum of 11230 Oe for X = 200 nm, then decreases. For X = 500 nm, the Zr_6Fe_{23}/Si(001) film exhibits significant decrease of M_s and H_a, around 81.2 emu/cm^3 and 10080 Oe, respectively. The strengthened exchange interaction between adjacent grains contributes to the increased remanence ratio $S^* = M_r/M_s$ from 0.51 to 0.74. The remanence ratio S* > 0.5 indicating good magnetic proprieties suggests strong exchange interactions between the adjacent crystallites [49–52]. The H_c variation as a function of Φ is defined by the following relation [53–55]: $\Phi_c = 9\kappa/2\pi M_s^2$, where $\kappa = (2k_B.K.T_C/\varrho)^{1/2}$ is the domain wall energy. T_C is Curie temperature, k_B is Boltzmann constant and ϱ is the lattice coefficient. The critical grain size value (Φ_c) from single domain to multi-domain is around 41.5 nm. This result is in good agreement with the experimental value for X = 200 nm. Figure 11 shows MFM images of Zr_6Fe_{23}/Si(001) films for X = 18 nm, 98 nm, 200 nm and 500 nm. The observed contrasts clearly show the dispersion of the magnetic domains in the analyzed surface. Each domain was separated by well-defined domain walls. A large number of uniform magnetic domains were observed in thickness X between 18 nm and 98 nm (Fig. 11a, b). For X = 18 nm, the image shows a complicated ripple domain pattern, did not evidence a major contribution of magnetic moments on the surface. For X

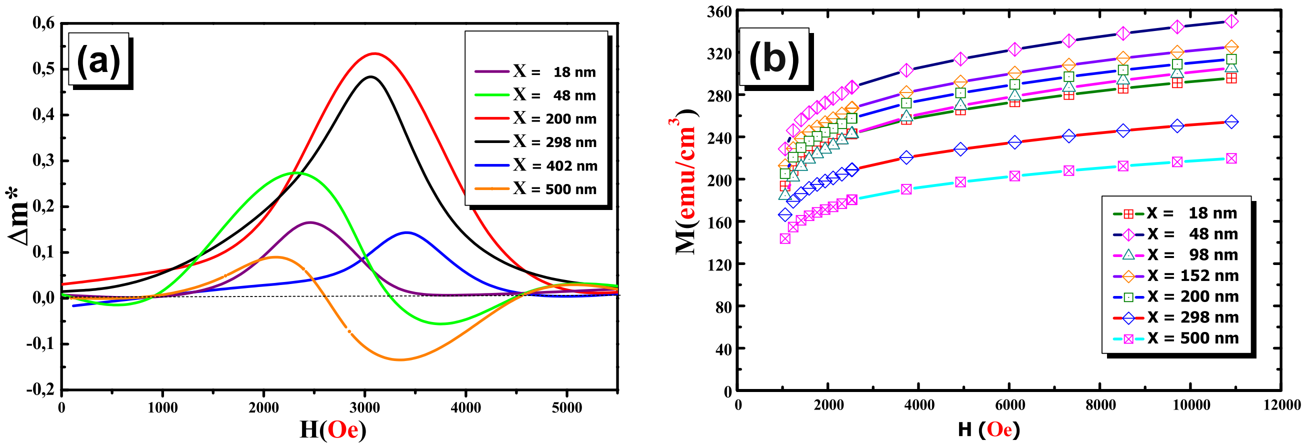

Fig. 10 **a** (Δm* curves of Zr_6Fe_{23}/Si(001) films with different X thickness (X = 18 nm, 48 nm, 200 nm, 298 nm, 402 nm and 500 nm). **b** The magnetization curve M(H) of Zr_6Fe_{23} /Si(001) films

Table 5 Coercivity H_c(Oe), maximum energy product $(BH)_{max}$(MGOe) and remanent magnetization M_r(emu/cm^3) for different X thickness

X(nm)	18	48	98	149	200	249	298	402	500
H_c	660	1780	2730	3010	3580	3120	2640	690	651
M_r	171	264	218	203	196	179	145	135	126
$(BH)_{max}$	0.912	0.942	1.56	2.03	2.45	2.16	1.94	1.62	0.38

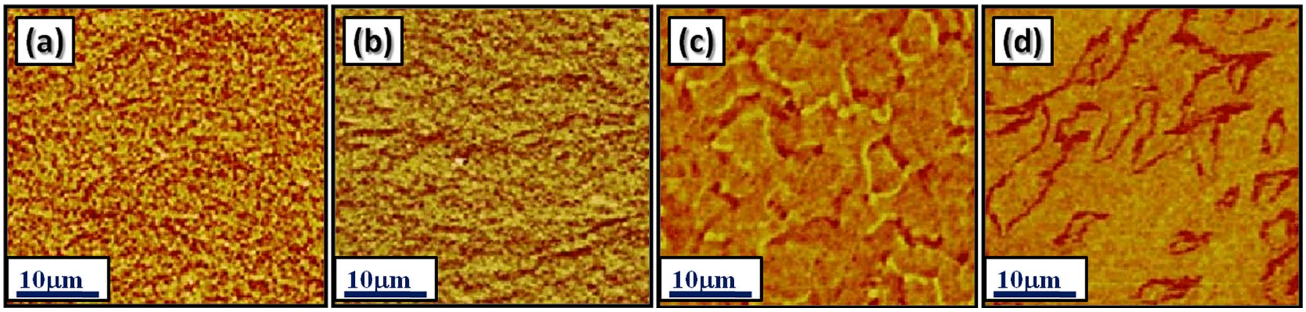

Fig. 11 MFM images of Zr_6Fe_{23}/Si(001) films for X = 18 nm (**a**), X = 98 nm (**b**), X = 200 nm (**c**) and X = 402 nm (**d**)

Table 6 The value of M_s(emu/cm^3), $S^* = M_r/M_s$ and H_a (Oe) of nanocrystalline Zr_6Fe_{23} /Si(001) film for different X thickness

X(nm)	M_s	S*	H_a
18	278	0.61	10100
48	355	0.68	11150
98	300	0.72	11160
149	301	0.67	11180
200	312	0.62	11230
249	238	0.75	11220
298	220	0.65	10600
402	215	0.62	10130
500	211	0.60	10080

= 200 nm, exhibited the single domains formation ranging in size 5–12 μm (Fig. 11c). For X ≥ 402 nm, the magnetic domains get bigger (Fig. 11d). This implies an increase in the size grains which are in a state with multiple magnetic domains. The magnetic structure change of Zr_6Fe_{23}/Si(001) film is the reason for the decrease in the magnetic anisotropy H_a and coercivity H_c as a function of X.

4 Conclusion

Nanocrystalline Zr_6Fe_{23} films of varying thickness X were deposited by RF magnetron sputtering process on Si(001) substrate. Grazing incidence X-ray diffraction (GIXRD) technique, atomic force microscopy (AFM), superconducting quantum interference device (SQUID), vibrating sample magnetometry (VSM) and magnetic force microscopy (MFM) were used to study the microstructural and magnetic properties of these films. The Zr_6Fe_{23}/Si(001) films show a single phase with a cubic structure of Th_6Mn_{23} type (Fm-3m space group). We showed the strong preferential orientation for thickness X between 18 and 402 nm. For X above 402 nm, multiple peaks are found indicating the polycrystalline nature of the films and textured along the (4 4 2), (5 3 3) and (6 6 0) orientations. The coercivity H_c, the squareness factor S* and the anisotropy field H_a were investigated as a function of X thickness and grain sizes D. The correlation between the microstructure, magnetic anisotropy parameters and intergrain exchange coupling (IEC) was analyzed. The excellent magnetic properties were found for thickness X = 200 nm: the coercivity H_c = 3580 Oe, maximum energy product $(BH)_{max}$ of 2.45 MGOe MGOe, magnetic anisotropy field H_a = 11230 Oe and Curie temperature $T_C \simeq 821$ K. The found results provide the fundamental reference for adapting the soft magnetic properties of Zr_6Fe_{23}/Si(001) films for high-density magnetic recording media and spintronic applications.

Acknowledgements This work is main supported by the Romanian Ministry of Research and Innovation (Romania) and the "Ministère de l'Enseignement Supérieur et de la Recherche Scientifique " (20PEJC 01-15) (Tunisia). The authors acknowledge the " Agence Universitaire de la Francophonie AUF " for his support.

References

1. A.P. Dalia, R. Fersi, J. Magn. Magn. Mater. **532**, 167874 (2021)
2. R. Fersi, H. Jabbalah, A. Bezergheanu, D. Patroi, C.B. Cizmas, L. Bessais, N. Mliki, Vacuum **174**, 109168 (2020)
3. R. Fersi, A. Bezergheanu, D. Patroic, C.B. Cizmas, L. Bessais, N. Mliki, J. Magn. Magn. Mater. **494**, 165816 (2020)
4. R. Fersi, N. Mliki, L. Bessais, Magnetochemistry **8**(2), 20 (2022)
5. R. Fersi, W. Bouzidi, A. Bezergheanu, C.B. Cizmas, L. Bessais, N. Mliki, J. Magn. Magn. Mater. **451**, 473 (2018)
6. C. Gao, H. Wan, G.C. Hadjipanayis, J. Appl. Phys. **67**, 4960 (1990)
7. Z. Altounian, E. Batalla, J.O.S. Olsen, J. Appl. Phys. **59**, 2364 (1986)
8. H. Drulis, W. Iwasieczko, V. Zaremba, J. Magn. Magn. Mater. **256**, 139 (2003)
9. A.M. Ghemawat, M. Foldeaki, R.A. Dunlap, R.C. O'Handley, IEEE Trans. Magn. **25**, 3312 (1989)
10. O.I. Bodak, B.V. Padlyaka, Y.V. Stadnyk, J. Pierre, A.V. Tkachuk, L.P. Romaka, Y.K. Gorelenko, J. Alloys Compd. **317**, 357 (2001)
11. A. D. Pelton, L. Leibowitz, R.A. Blomquist, J. Nucl. Mater. 201 218
12. K. Bhanumurthy, Scr. Metall. Mater. **28**, 753 (1993)
13. N. Mattern, W.X. Zhang, S. Roth, H. Reuther, C. Baehtz, M. Richter, J. Phys.: Condens. Matter **19**, 376202 (2007)
14. P. Warren, J.B. Forsyth, G.J. McIntyre, N. Bernhoeft, J. Phys.: Condens. Matter **4**, 5795 (1992)

15. L. Leibowitz, R.A. Blomquist, J. Nucl. Mater. **201**, 218 (1993)
16. C. Servant, C. Guéneau, I.J. Ansara, Alloys Compd. **220**, 19 (1995)
17. V. N. Svechnikov, V. M. Pan, A. T. Russ Spektor. J. Inorg. Chem. 8, 1106, 963
18. K. Bakkari, R. Fersi, H. El Kébir, L. Bessais, N. Mliki, J. Phys.: Condens. Matter **9**, 30 (2018)
19. A. R. Chezan, C. B. Craus, N. G. Chechenin, L. Niesen, and D. O. Boerma, phys. stat. sol. (a) 189, No. 3 (2002) 833
20. A. Chakraborty, K.R. Mountfield, G.H. Bellesis, D.N. Lambeth, M.H. Kryder, J. Appl. Phys. **80**, 1012 (1996)
21. Y. Kitano, H. Horio, A. Ido, T. Watanabe, M. Komai, K. Takagi, Intermetallics **4**, S209–S213 (1996)
22. D. Kaoumi, A. T. Motta, R. C. Birtcher, Nucl. Instr. and Meth. in Phys. Res. B 242 (2006) 490
23. A. T. Motta, A. Paesano. Jr., R. C. Birtcher, L. Amaral, Nucl. Instr. and Meth. in Phys. Res. B 175-177 (2001) 521
24. R.A. Dunlap, D.A. Small, G.R. MacKay, J.W. O'Brien, J.R. Dahn, Z.H. Cheng, Can. J. Phys. **78**, 211 (2000)
25. M. Phejar, V. Paul-Boncour, L. Bessais, Intermetallics **18**, 2301–2307 (2010)
26. H. Rietveld, J. Appl. Crystallogr. **2**, 65 (1969)
27. J. Rodrguez-Carvajal, Phys. B **192**, 55 (1993)
28. L. Bessais, C. Djega-Mariadassou, Phys. Rev. B **63**, 054412 (2001)
29. https://www.bruker.com/fr/products-and-solutions/diffractometers-and-scattering-systems/x-ray-diffractometers/diffrac-suite-software/diffrac-leptos.html
30. A. Ulyanenkov, K. Omote, J. Harada, Physica B Condens. Matter **283**, 237 (2000)
31. R. Fersi, N. Mliki, M. Cabié, L. Bessais, Phys. Status Solidi (a) **211**(4), 910 (2014)
32. R. Fersi, N. Mliki, L. Bessais, R. Guetari, V. Russier, M. Cabié, J. Alloys Compd. **522**, 14 (2012)
33. R. Fersi, N. Mliki, L. Bessais, J. Magn. Magn. Mater. **465**, 220 (2018)
34. R. Fersi, W. Bouzidi, N. Mliki, L. Bessais, Intermetallics **100**, 181 (2018)
35. R. Fersi, M. Cabié, N. Mliki, L. Bessais, Int. J. Hydrog. Energy. 44, Issue 39 (2019) 22011
36. H. Jaballah, W. Bouzidi, R. Fersi, N. Mliki, L. Bessais, J. Phys. Chem. Solids **161**, 110438 (2022)
37. R. Bez, R. Fersi, K. Zehani, J. Moscovici, L. Bessais, N. Mliki, E. Fonda, A. Michalowicz, J. Alloy. Compd. **666**, 317 (2016)
38. L. Bessais, R. Fersi, M. Cabié, N. Mliki, MRS Online Proceedings Library (OPL) 1471 (2012)
39. X. Zhang, Y. Lao, J. Sklenar, N.S. Bingham, J.T. Batley, J.D. Watts, C. Nisoli, C. Leighton, P. Schiffer, APL Mater. **7**, 111112 (2019)
40. Y. Li, L. Peng, J. Magn. Magn. Mater. **323**(5), 475 (2011)
41. A. Kaibi, A. Guittoum, R.M. Öksüzogluc, A.M. Yagcic, M. Boudissad, M. Kechouanea, Appl. Surf. Sci. **350**, 50 (2015)
42. T. Stefan, H. Jurgen, J. Magn. Magn. Mater. 154, no.1, 254, 1996
43. L. Ning, L. Baohe, F. Chun, L. Minghua, Y. Guanghua, J. Rare. Earth, 30, no.5, 446, 2012
44. Z. Yamkane, R. Fersi, F.Z. Rachid, R. Moubah, H. Lassri, N. Mliki, L. Bessais, J. Magn. Magn. Mater. **449**, 461 (2018)
45. L. Néel, Rep. Prog. Phy. Radium **9**, 193 (1948)
46. Z. Zhang, X. Song, W. Xu, Acta Mater. **59**, 1808 (2011)
47. Z. Yamkane, R. Fersi, F. Z. Rachid, R. Moubah, H. Lassri, N. Mliki, S. Alleg, M. Sajieddine, L. Bessais, SPIN (2020) 2050016
48. H. Lassri, M. Tlemçani, M. Slimani, S. Sayouri, M. Abid, H. Houmada, A. Mikou, Phys. B **239**, 274 (1997)
49. R. Fersi, N. Mliki, L. Bessais, IOP Conf. Series: Materials Science and Engineering, 28 (2012) 012014
50. R. Fersi, M. Cabié, N. Mliki, L. Bessais, J. Alloys Compd. **576**, 415 (2013)
51. L. Bessais, R. Fersi, M. Cabié, N. Mliki, TMS2013 Supplemental Proceedings, 2013, 97-104
52. R. Fersi, N. Mliki, L. Bessais, EPJ Web of Conferences **29**, 00018 (2012)
53. B.D. Cullity, A. Wesley, *Reading* (Mass, USA, 1974)
54. M. George, A.M. John, S.S. Nair, P.A. Joy, M.R. Anantharaman, J. Magn. Magn. Mater. **302**(1), 190 (2006)
55. C. Caizer, Mater. Sci. Eng., B, 100, no.1 (2003) 63